

Early Stage of Superradiance from Bose-Einstein Condensates

L. F. Buchmann,^{1,2} G. M. Nikolopoulos,² O. Zobay,³ and P. Lambropoulos^{2,1}

¹*Department of Physics, University of Crete,
P.O. Box 2208, Herakleion 710 03, Crete, Greece*

²*Institute of Electronic Structure and Laser,
Foundation of Research and Technology Hellas,
P.O. Box 1527, Herakleion 711 10, Crete, Greece*

³*School of Mathematics, University of Bristol,
University Walk, Bristol BS8 1TW, UK*

(Dated: April 15, 2018)

Abstract

We investigate the dynamics of matter and optical waves at the early stage of superradiant Rayleigh scattering from Bose-Einstein Condensates. Our analysis is within a spatially dependent quantum model which is capable of providing analytic solutions for the operators of interest. The predictions of the present model are compared to the predictions of a closely related mean field model, and we provide a procedure that allows one to calculate quantum expectation values by averaging over semiclassical solutions. The coherence properties of the outgoing scattered light are also analyzed, and it is shown that the corresponding correlation functions may provide detailed information about the internal dynamics of the system.

PACS numbers: 03.75.Nt,67.85.-d,37.10.Vz,42.50.Ct

I. INTRODUCTION

Superradiance in general terms refers to enhanced emission from an ensemble of radiators. It was first predicted by Dicke in 1954 [1] and since then experimentally confirmed to occur in many systems, such as gases of excited atoms, molecules or quantum dots [2, 3]. Recently, superradiant scattering off an elongated atomic Bose-Einstein condensate (BEC) has received much theoretical [4–7] and experimental [8–10] attention. There are many similarities, but also important differences between the “conventional” superradiance, for example off excited gases, and the superradiance off atomic condensates. Atoms in a BEC have a narrow momentum distribution, and thus the recoil they experience during the absorption and emission of photons has a profound impact on their momentum distribution, leading to distinct atomic scattering patterns.

In the case of superradiant Rayleigh scattering off BECs, different regimes of parameters have been identified, which are characterized by distinct atomic patterns. Mean-field models were found to successfully predict and explain such patterns, as well as the transition between different regimes, provided the models include spatial effects [4, 6]. The main drawback of such models, however, is that one has to “seed” the equations of motion, in order to start their evolution in time. The seeding introduces some ambiguity in the solutions, which is expected to become less important for large times due to the fast growth of the population in the various optical and matter-wave modes. In contrast to the mean-field models, the quantum models that have been used in this context, are capable of describing accurately the startup of the process, but do not take into account spatial propagation effects [5, 7].

In a recent work [11], we investigated the coherence properties of matter waves produced in superradiant scattering off BECs, and analyzed the type of spatial correlations involved. This has been possible in the framework of a spatially-dependent quantum model, which can describe quantum fluctuations while capturing spatial effects, essential for a full understanding of the process. The purpose of the present paper is to provide a full derivation of the model used in [11], and to obtain further detailed insights into the dynamics of the system. We explicitly compare our results to those obtained within a related mean-field model, and show that for a large collection of condensed atoms, the effect of quantum fluctuations on various observable quantities can be obtained by averaging over ensembles of semiclassical solutions (“trajectories”). Finally, we discuss the temporal coherence of the scattered light,

which is shown to carry information about the internal dynamics of the system.

II. THE MODEL

The system under consideration pertains to a BEC elongated along the z -axis, consisting of N atoms. A linearly polarized laser with frequency $\omega_l = k_l c$, far detuned from the closest atomic transition by a value of δ , is illuminating the cloud along the x -axis. Assuming two-level atoms and adiabatically eliminating the excited atomic state, the Maxwell-Schrödinger equations for the system read [3, 12]

$$i\hbar \frac{\partial}{\partial t} \hat{\psi}(\mathbf{x}, t) = -\frac{\hbar^2}{2M} \Delta \hat{\psi}(\mathbf{x}, t) + \frac{[\mathbf{d} \cdot \hat{\mathbf{E}}^{(-)}(\mathbf{x}, t)][\mathbf{d} \cdot \hat{\mathbf{E}}^{(+)}(\mathbf{x}, t)]}{\hbar\delta} \hat{\psi}(\mathbf{x}, t), \quad (1a)$$

$$\frac{\partial^2 \hat{\mathbf{E}}^{(\pm)}(\mathbf{x}, t)}{\partial t^2} = c^2 \Delta \hat{\mathbf{E}}^{(\pm)}(\mathbf{x}, t) - \frac{1}{\varepsilon_0} \frac{\partial^2 \hat{\mathbf{P}}^{(\mp)}(\mathbf{x}, t)}{\partial t^2}, \quad (1b)$$

with the atomic polarization

$$\hat{\mathbf{P}}^{(-)}(\mathbf{x}, t) = -\mathbf{d} \hat{\psi}^\dagger(\mathbf{x}, t) \frac{\mathbf{d} \cdot \hat{\mathbf{E}}^{(+)}(\mathbf{x}, t)}{\hbar\delta} \hat{\psi}(\mathbf{x}, t), \quad (1c)$$

satisfying $\mathbf{P}^{(+)} = \mathbf{P}^{(-)\dagger}$. The operators $\hat{\mathbf{E}}^{(\pm)}(\mathbf{x}, t)$ are the positive and negative frequency parts of the electromagnetic field, while $\hat{\psi}(\mathbf{x}, t)$ is the operator describing the ground state of the atoms, which have mass M and dipole moment \mathbf{d} . In writing Eqs. (1) we have neglected the external trapping potential as well as atomic interactions, which both do not play a significant role for the timescales of interest. Due to the coherent nature of the condensate, successive Rayleigh scattering events are strongly correlated and lead to collective superradiant behavior. As a result of the cigar-shape of the condensate, the gain is largest when the scattered photons leave the condensate along its long axis, traveling in the so called *endfire modes* with wave vectors $\mathbf{k} \approx \pm k_l \mathbf{e}_z$. A condensate atom can scatter a laser photon into the endfire modes, experiencing a recoil $\hbar\mathbf{q} \approx \hbar(k_l \mathbf{e}_x - \mathbf{k})$. On the other hand, it can also scatter a photon from the endfire modes into the laser mode, in which case its momentum changes by $\hbar\mathbf{q} \approx \hbar(-k_l \mathbf{e}_x + \mathbf{k})$. These processes lead to the formation of two pairs of atomic *side-modes*, consisting of counterpropagating atoms with a narrow momentum spread (compared to k_l). Of course, atoms within these side-modes can also scatter photons, thereby acquiring higher momenta, but since we are interested in the early stage of the process, we consider only first order sidemodes to be populated.

Neglecting any coupling *between* counterpropagating photonic endfire modes, the system becomes symmetric with respect to the x -axis. We can thus focus on the endfire modes with $\mathbf{k} \approx +k\mathbf{e}_z$ and on the two atomic side-modes (with central momenta $\hbar\mathbf{q} = \pm\hbar(k_l\mathbf{e}_x - k\mathbf{e}_z)$) that are coupled to them. Due to the strong confinement along the x - and y -axis, we can assume the transverse profiles of the matter field $\psi_\perp(x, y)$ to be well described by a classical function, independent of the z -coordinate [6]. Assuming a Fresnel number close to unity for the electromagnetic fields, we can apply the same approximation for the transverse part of the radiation field $u_\perp(x, y)$, effectively reducing the problem to one dimension.

We expand the field operators as

$$\hat{\psi}(\mathbf{x}, t) = \psi_\perp(x, y) \sum_{j=-1}^1 \hat{\psi}_j(z, t) e^{ij(k_l x - kz) - i\omega_j t} \quad (2a)$$

$$\hat{\mathbf{E}}^{(+)}(\mathbf{x}, t) = \frac{\mathcal{E}_0}{2} \mathbf{e}_y e^{i(k_l x - \omega_l t)} + u_\perp(x, y) \hat{E}_+^{(+)}(z, t) \mathbf{e}_y, \quad (2b)$$

where $\omega_{\pm 1} = \hbar(k_l^2 + k^2)/2M$ and $\omega_0 = 0$. The matter-wave operator is split up in three parts, describing the two side-modes ($j = \pm 1$) and the BEC at rest ($j = 0$),

$$\hat{\psi}_j(z, t) = e^{i\omega_j t} \sum_{p \in \Delta_0} \frac{e^{ipz}}{\sqrt{L}} \hat{c}_{-jk+p}(t), \quad (3a)$$

where Δ_0 is the interval $(-k/2, k/2)$ in k -space, L is the length of the BEC and \hat{c}_p annihilates an atom with momentum $\hbar p$. Since the BEC at rest remains practically undepleted it can be treated as a time independent classical function and hence we can set $\hat{\psi}_0(z, t) \equiv \psi_0(z)$.

Similarly, we expand the endfire mode operator as

$$\begin{aligned} \hat{E}_+^{(+)}(\mathbf{z}, t) &= i e^{i(kz - \omega t)} \sum_{p \in \Delta_0} \sqrt{\frac{\hbar\omega_{k+p}}{2\varepsilon_0}} \frac{1}{\sqrt{L}} e^{ipz} e^{i\omega t} \hat{a}_{k+p}(t) \\ &\approx \sqrt{\frac{\hbar\omega}{2\varepsilon_0}} e^{i(kz - \omega t)} \hat{e}_+(z, t), \end{aligned} \quad (3b)$$

where \hat{a}_p is the photon annihilation operator. The frequencies ω_{k+p} are approximated by $\omega = k/c$, the frequency of the scattered photons, and can therefore be taken out of the sum. This approximation is justified by the fact that dominant contributions to the sum come from momenta of order $1/L$, which is several orders of magnitude smaller than k .

The one-dimensional field operators satisfy the commutation relations

$$\left[\hat{\psi}_i(z_1, t), \hat{\psi}_j^\dagger(z_2, t) \right] = \delta_{ij} \delta_\Delta(z_1 - z_2), \quad (4a)$$

$$\left[\hat{e}_+(z_1, t), \hat{e}_+^\dagger(z_2, t) \right] = \delta_\Delta(z_1 - z_2), \quad (4b)$$

$$\left[\hat{e}_+(z, t_1), \hat{e}_+^\dagger(z, t_2) \right] = \frac{1}{c} \delta_\Delta(t_1 - t_2), \quad (4c)$$

where $\delta_\Delta(z)$ is a distribution with width of order $1/k$ and δ_{ij} denotes the Kronecker delta [18]. Inserting expansions (2) in the equations of motion (1), we can make some further simplifications. Considering that k_l is about a factor of 10 smaller than the extent of the BEC cloud along the strongly confined axes, the two transverse functions $\psi_\perp(x, y)e^{\pm ik_l x}$ are mutually orthogonal to a very good degree of approximation. Hence we can project on either of the two side-mode operators by multiplying with the complex conjugate of the corresponding transverse function and integrate over the variables x and y .

Since we included the phase factors arising from the free time evolution in the definition of the operators, we can apply the slowly-varying-envelope approximation (SVEA), which yields the equations

$$\frac{\partial \hat{\psi}_{+1}^\dagger(\xi, \tau)}{\partial \tau} = i\kappa \hat{e}_+(\xi, \tau) \psi_0^*(\xi), \quad (5a)$$

$$\frac{\partial \hat{\psi}'_{-1}(\xi, \tau)}{\partial \tau} = -i\kappa \hat{e}_+(\xi, \tau) \psi_0(\xi) - 2i\hat{\psi}'_{-1}(\xi, \tau), \quad (5b)$$

$$\begin{aligned} \frac{\partial \hat{e}_+(\xi, \tau)}{\partial \tau} + \chi \frac{\partial \hat{e}_+(\xi, \tau)}{\partial \xi} = & -i \left[\kappa \psi_0(\xi) \hat{\psi}_{+1}^\dagger(\xi, \tau) \right. \\ & \left. + \kappa \hat{\psi}'_{-1}(\xi, \tau) \psi_0^*(\xi) \right]. \end{aligned} \quad (5c)$$

Here we have defined $\hat{\psi}'_{-1}(\xi, \tau) = e^{-2i\tau} \hat{\psi}_{-1}(\xi, \tau)$ and rescaled length and time to dimensionless units

$$\xi = k_l z, \quad \tau = 2\omega_r t, \quad (6)$$

where $\omega_r = \hbar k_l^2 / 2M$. Accordingly, the fields are rescaled as

$$\hat{e}_+(\xi, \tau) \equiv \frac{1}{\sqrt{k_l}} \hat{e}_+(z, t) \quad \hat{\psi}_j(\xi, \tau) \equiv \frac{1}{\sqrt{k_l}} \hat{\psi}_j(z, t),$$

and the speed of light becomes $\chi \equiv \frac{ck}{2\omega_r}$. The effective one-dimensional coupling is given by $\kappa = g\sqrt{k_l L} / (2\omega_r)$ with

$$g = \frac{|\mathbf{d} \cdot \mathbf{e}_y|^2 \mathcal{E}_0}{\hbar^2 \delta} \sqrt{\frac{\hbar \omega}{2\epsilon_0 L}} \int dx dy u_\perp(x, y) \psi_\perp^2(x, y).$$

The SVEA pertained to neglecting derivatives of slowly varying functions in order to arrive at Eqs. (5a), (5b). For Eq. (5c), we have kept first order derivatives, but neglected terms proportional to $\hat{e}_+(z, t)$ in comparison to the laser field. The frequencies in our system satisfy $\omega_{\pm 1} \ll \omega_l, \omega$ and thus we only kept time derivatives involving $e^{-i\omega t}$ and approximated $\omega \approx \omega_l$.

Backwards recoiling atoms are a particular feature of superradiant Rayleigh scattering off condensates. The physical process underlying the backwards modes violates energy conservation by an amount $\Delta E \simeq 4\hbar\omega_r$. Thus, according to Heisenberg uncertainty principle, it can take place only for times shorter than a critical time $t_c = \hbar/\Delta E$ [9], which, in our units, is given by

$$\tau_c = 0.5. \quad (7)$$

For such short pulses, and for sufficiently high power one typically observes an X-shaped pattern for the distribution of the atomic side modes with the initial BEC in the center and the recoiling atoms moving both in and against the direction of the applied laser pulse (*Kapitza-Dirac* or *strong-pulse regime*). On the other hand, for weaker pulses with duration longer than τ_c , the distribution of the side modes exhibits a fan pattern, involving mainly forward recoiling atoms (*Bragg* or *weak pulse regime*). If we neglect the atomic backwards sidemode altogether, Eqs. (5) become formally equivalent to descriptions of “conventional” superradiance from excited atomic gases [1].

Finally, the equations of motion (5) can be derived from the effective, self-adjoint Hamiltonian

$$\hat{H} = \int d\xi \left(-\frac{i}{2} \hat{e}_+^\dagger \frac{\partial \hat{e}_+}{\partial \xi} + \hat{\psi}_{-1}^\dagger \hat{\psi}'_{-1} + \kappa \psi_0 \hat{e}_+^\dagger \hat{\psi}_{+1}^\dagger + \kappa \psi_0^* \hat{e}_+^\dagger \hat{\psi}'_{-1} + \text{h.c.} \right), \quad (8)$$

where “h.c.” stands for the Hermitian conjugate. The system being effectively hamiltonian guarantees conservation of the commutation relations (4) for all times. Differentiating the atomic densities

$$n_j(\xi, \tau) = \langle \hat{\psi}_j^\dagger(\xi, \tau) \hat{\psi}_j(\xi, \tau) \rangle \quad (9a)$$

and the photon density

$$\mathfrak{J}(\xi, \tau) = \langle \hat{e}_+^\dagger(\xi, \tau) \hat{e}_+(\xi, \tau) \rangle \quad (9b)$$

with respect to time, using Eqs. (5) and adding up the resulting three equations, we find the continuity equation

$$\frac{\partial}{\partial \tau} [n_{+1}(\xi, \tau) - n_{-1}(\xi, \tau) - \mathfrak{J}(\xi, \tau)] = \chi \frac{\partial}{\partial \xi} \mathfrak{J}(\xi, \tau). \quad (10)$$

Let us now integrate this equation over time from 0 to τ and over space from one end of the condensate at $\xi = 0$ to the other end at $\xi = \Lambda \equiv k_l L$. Assuming that side-mode and photon populations vanish at $\tau = 0$, we find

$$\mathcal{N}_{+1}(\tau) - \mathcal{N}_{-1}(\tau) - \mathcal{I}_{\text{in}}(\tau) = \mathcal{I}_{\text{out}}(\tau), \quad (11)$$

where we have defined the total populations for the atoms

$$\mathcal{N}_j(\tau) = \int_0^\Lambda d\xi n_j(\xi, \tau), \quad (12a)$$

and the photons

$$\mathcal{I}_{\text{in}}(\tau) = \int_0^\Lambda d\xi \mathfrak{J}(\xi, \tau), \quad (12b)$$

$$\mathcal{I}_{\text{out}}(\tau) = \chi \int_0^\tau d\tau' \mathfrak{J}(\Lambda, \tau'). \quad (12c)$$

In words, Eq. (11) expresses that at any time τ , the number of forward-recoiling atoms $\mathcal{N}_+(\tau)$, is equal to the sum of backwards recoiling atoms $\mathcal{N}_-(\tau)$, and endfire photons inside and outside the BEC volume, denoted by $\mathcal{I}_{\text{in(out)}}(\tau)$. It is therefore consistent with the intuitive picture of the underlying process and it may serve as a convenient check for numerical simulations.

III. SOLUTIONS OF THE EQUATIONS OF MOTION

We can use the Laplace transform to find exact solutions to the system (5) in terms of the operators evaluated at the boundary of their domain – i.e. at $\xi = 0$ and $\tau > 0$ or vice versa at $\xi > 0$ and $\tau = 0$. More details on this procedure are given in the appendix. The solutions read

$$\begin{aligned} \hat{e}_+(\xi, \tau) = & \int_0^\tau d\tau' \hat{e}_+(0, \tau') F_{0,0}(\gamma_{\xi,0}, \tau - \tau' - \beta_{\xi,0}) - \frac{i\kappa}{\chi} \int_0^\xi d\xi' \left[\psi_0(\xi') \hat{\psi}'_{+1}(\xi', 0) F_{1,0}(\gamma_{\xi,\xi'}, \tau - \beta_{\xi,\xi'}) \right. \\ & \left. + \psi_0^*(\xi') \hat{\psi}'_{-1}(\xi', 0) F_{0,1}(\gamma_{\xi,\xi'}, \tau - \beta_{\xi,\xi'}) + \frac{i}{\kappa} \hat{e}_+(\xi', 0) F_{0,0}(\gamma_{\xi,\xi'}, \tau - \beta_{\xi,\xi'}) \right], \end{aligned} \quad (13a)$$

$$\begin{aligned} \hat{\psi}'_{+1}(\xi, \tau) = & i\kappa\psi_0^*(\xi) \int_0^\tau d\tau' \hat{e}_+(0, \tau') F_{1,0}(\gamma_{\xi,0}, \tau - \tau' - \beta_{\xi,0}) + \hat{\psi}'_{+1}(\xi, 0) \\ & + \frac{\kappa^2}{\chi} \psi_0^*(\xi) \int_0^\xi d\xi' \left[\psi_0(\xi') \hat{\psi}'_{+1}(\xi', 0) F_{2,0}(\gamma_{\xi,\xi'}, \tau - \beta_{\xi,\xi'}) \right. \\ & \left. + \psi_0^*(\xi') \hat{\psi}'_{-1}(\xi', 0) F_{1,1}(\gamma_{\xi,\xi'}, \tau - \beta_{\xi,\xi'}) + \frac{i}{\kappa} \hat{e}_+(\xi', 0) F_{1,0}(\gamma_{\xi,\xi'}, \tau - \beta_{\xi,\xi'}) \right], \end{aligned} \quad (13b)$$

$$\begin{aligned} \hat{\psi}'_{-1}(\xi, \tau) = & -i\kappa\psi_0(\xi) \int_0^\tau d\tau' \hat{e}_+(0, \tau') F_{0,1}(\gamma_{\xi,0}, \tau - \tau' - \beta_{\xi,0}) + e^{-i2\tau} \hat{\psi}'_{-1}(\xi, 0) \\ & - \frac{\kappa^2}{\chi} \psi_0(\xi) \int_0^\xi d\xi' \left[\psi_0(\xi') \hat{\psi}'_{+1}(\xi', 0) F_{1,1}(\gamma_{\xi,\xi'}, \tau - \beta_{\xi,\xi'}) \right. \\ & \left. + \psi_0^*(\xi') \hat{\psi}'_{-1}(\xi', 0) F_{0,2}(\gamma_{\xi,\xi'}, \tau - \beta_{\xi,\xi'}) + \frac{i}{\kappa} \hat{e}_+(\xi', 0) F_{0,1}(\gamma_{\xi,\xi'}, \tau - \beta_{\xi,\xi'}) \right], \end{aligned} \quad (13c)$$

where we have introduced

$$\beta_{\xi,\xi'} = \frac{\xi - \xi'}{\chi}, \quad \gamma_{\xi,\xi'} = \frac{\kappa^2}{\chi} [\rho(\xi) - \rho(\xi')],$$

with $\rho(\xi) = \int_0^\xi d\xi' |\psi_0(\xi')|^2$. The functions $F_{\mu,\nu}(u, v)$ are defined as

$$F_{\mu,\nu}(u, v) = \mathcal{L}_{p \rightarrow v}^{-1} \left\{ \frac{e^{u/p} e^{-u/(p+2i)}}{p^\mu (p+2i)^\nu} \right\},$$

where $\mathcal{L}_{p \rightarrow v}^{-1}$ denotes the inverse Laplace transform. One can check easily that Eqs. (13) indeed are solutions to the system (5) by using recursion relations for the functions $F_{\mu,\nu}$ which are given in the appendix, alongside the explicit expressions of the functions themselves. Explicit expressions for the functions $F_{\mu,\nu}(u, v)$ appearing in (13) are given in the appendix. They are combinations and integrals over combinations of Bessel Functions. It shall only be noted here, that all of the terms appearing in $F_{\mu,\nu}(u, v)$ contain Heaviside step functions $\Theta(v)$, except one term in $F_{0,0}(u, v)$, which is simply the Dirac delta function with argument v .

We note that in Eqs. (13), all time arguments are shifted by the value $\beta_{\xi,\xi'}$, which is the time a photon needs to travel from ξ' to ξ . Using the step functions in the solutions to change the range of the integrals and assuming free light propagation outside the condensate we can reformulate Eqs. (13), such that they involve only spatial integrals ranging from $\xi - \tau\chi$ to ξ .

This is a consequence of the finite speed of light, allowing atoms at ξ only to be influenced by atoms within a range $\xi - \tau\chi$. Such retardation effects are very small in the system at hand and can be neglected for all practical purposes. We can do so formally by letting $\chi \rightarrow \infty$, which implies $\beta_{\xi,\xi'} \rightarrow 0$, and neglecting all the terms proportional to $\hat{e}_+(\xi', 0)$ in the spatial integrals of Eqs. (13). The resulting solutions will still describe the system correctly, since the effects of this approximation are expected to be of the order of $\Lambda/\chi \approx 10^{-7}$, and are thus too small to be noted in typical BEC experiments. Formally, this approximation will lead to a nonzero initial photon population within the BEC, which we can safely neglect due to its small value.

Equations (13) can be simplified considerably if we neglect backward recoiling atoms. Neglecting retardation effects, we obtain

$$\begin{aligned} \hat{e}_+(\xi, \tau) &= \int_0^\tau d\tau' \hat{e}_+(0, \tau') F_0(\gamma_{\xi,0}, \tau - \tau') \\ &\quad - \frac{i\kappa}{\chi} \int_0^\xi d\xi' \psi_0(\xi') \hat{\psi}_{+1}^\dagger(\xi', 0) F_1(\gamma_{\xi,\xi'}, \tau) \end{aligned} \quad (14a)$$

$$\begin{aligned} \hat{\psi}_{+1}^\dagger(\xi, \tau) &= i\kappa\psi_0^*(\xi) \int_0^\tau d\tau' \hat{e}_+(0, \tau') F_1(\gamma_{\xi,0}, \tau - \tau') + \hat{\psi}_{+1}^\dagger(\xi, 0) \\ &\quad + \frac{\kappa^2}{\chi} \psi_0^*(\xi) \int_0^\xi d\xi' \psi_0(\xi') \hat{\psi}_{+1}^\dagger(\xi', 0) F_2(\gamma_{\xi,\xi'}, \tau), \end{aligned} \quad (14b)$$

where $F_\mu(u, v) = \mathcal{L}_{p \rightarrow v}^{-1} \{e^{u/p} p^{-\mu}\}$; explicit formulas for $F_\mu(u, v)$ are given in the appendix. It is worth emphasizing that these equations are consistent with the equations other authors derived to describe conventional superradiance [13].

Assuming that the initial population of the atomic side modes is zero, we can find the expectation value of any correlation function pertaining to electromagnetic- or matter-wave fields using Eqs. (4) and (13) and calculating the occurring integrals numerically. For the numerical calculations, we assumed the BEC to consist of $N = 10^6$ Thomas-Fermi distributed ^{87}Rb atoms, such that $\psi_0 = \sqrt{\Theta(z)N6(Lz - z^2)/L^3}$ with $L = 130\mu\text{m}$. We used a spatial grid of 400 points. For the incoming laser we chose a rectangular profile and a wavenumber $k_l = 8.05 \times 10^6 \text{m}^{-1}$, which results in a dimensionless length of the BEC of $\Lambda \sim 1000$. Coupling strengths are conveniently expressed in terms of the *superradiant gain* $\Gamma = \kappa^2 N/\chi$, whose value separates the two regimes identified by experimental observations of superradiance from condensates [10]. Typically, the weak coupling regime is characterized by $g \sim 10^5 \text{s}^{-1}$ and $\Gamma \sim 1$, while for $g \sim 10^6 \text{s}^{-1}$ and $\Gamma \gg 1$ the system is in the strong coupling

regime. In our calculations, we chose $\Gamma = 1$ and $\Gamma = 100$ for the two regimes.

IV. QUANTUM VS. MEAN FIELD DESCRIPTION

Various aspects of the strong and weak-coupling regimes have been described successfully within a mean-field (MF) model [6], which is closely related to the present quantum model given by Eqs. (5). In fact, one arrives at Eqs. (15) of [6] by adapting the approximations of the present quantum model and replacing the operators in Eqs. (5) with their expectation values, treating them as classical fields. Consequently, we will refer to the solutions of the mean field model as $\psi_j(\xi, \tau) \equiv \langle \hat{\psi}_j(\xi, \tau) \rangle$ and $e_+(\xi, \tau) \equiv \langle \hat{e}_+(\xi, \tau) \rangle$. Due to the generality of the Laplace transform, these solutions look exactly like Eqs. (13), but with the operators replaced by classical fields.

Both models take into account spatial effects, which have been shown to play a major role in Rayleigh superradiance from condensates [6]. Given, however, that our system is initially prepared in the vacuum state, both $\psi_j(\xi, \tau)$ and $e_+(\xi, \tau)$ will remain zero throughout the evolution of the system, because their equations of motion [see Eqs. (13)], are not coupled to any operator with non-zero expectation value [i.e., $\psi_j(\xi, 0) = 0$ and $e_+(\xi, 0) = 0$]. This is a major drawback of the MF model, which can be resolved by seeding either of the modes i.e., assigning a non-zero initial value to either $\psi_j(\xi, 0)$ or $e_+(\xi, 0)$. The arbitrariness of such a seeding introduces some ambiguity regarding the dynamics of the system for short times, where all the modes are scarcely populated. The MF model is expected to be valid for longer times, where the fast growth of the population in the modes eliminates any ambiguity caused by the initial seeding. At such times, the MF model explains reasonably well various experimental observations [6]. Our purpose in this section is to investigate how accurately one can describe the onset of superradiance from condensates, in the framework of this MF model. To this end, we will compare the predictions of the MF model for various observables, to the corresponding predictions of the quantum model, which is capable of describing accurately initial quantum mechanical fluctuations, and does not require any seeding.

A. Atomic Densities and Populations

A rather convenient observable in a superradiant scattering process from a BEC, is the atomic density of the sidemode j , denoted by $n_j(\xi, \tau)$. After turning off the atomic trap, atoms in the sidemodes separate from the BEC at rest due to their additional momentum and form observable scattering patterns [9].

In the quantum model, we have $n_j(\xi, \tau) = \langle \hat{\psi}_j^\dagger(\xi, \tau) \hat{\psi}_j(\xi, \tau) \rangle$, which in view of Eqs. (13) yields

$$n_{-1}(\xi, \tau) = \Gamma^2 |\varphi(\xi)|^2 \int_0^\xi d\xi' |\varphi(\xi')|^2 |F_{1,1}(\gamma_{\xi, \xi'}, \tau)|^2, \quad (15a)$$

$$n_{+1}(\xi, \tau) = n_{-1}(\xi, \tau) + \Gamma |\varphi(\xi)|^2 \int_0^\tau d\tau' |F_{1,0}(\gamma_{\xi, 0}, \tau')|^2, \quad (15b)$$

where $\varphi(\xi) = \psi_0(\xi)/\sqrt{N}$. In the MF model, expectation values are defined as the squared modulus of the classical functions, i.e. $n_j(\xi, \tau) = |\psi_j(\xi, \tau)|^2$. By means of these quantities, we can directly compare the two models.

As a first step, let us neglect for the time being backward recoiling atoms. In this case one can obtain analytic expressions for the atomic densities, which acquire particularly simple forms for a flat BEC [i.e., for $\psi_0(\xi) = \sqrt{N/\Lambda}$]. Equation (15b) reduces to

$$n_{+1}(\xi, \tau) = \bar{\Gamma} \tau \left[I_0^2(2\sqrt{\bar{\Gamma}\xi\tau}) - I_1^2(2\sqrt{\bar{\Gamma}\xi\tau}) \right], \quad (16)$$

with $\bar{\Gamma} = \Gamma/\Lambda$, whereas within the MF model one obtains

$$n_{+1}(\xi, \tau) = \frac{|\psi_{+1}(\xi, 0)|^2}{\Lambda} I_0^2(2\sqrt{\bar{\Gamma}\xi\tau}). \quad (17)$$

Note here that the prefactor of the Bessel functions in the case of the quantum model is a linear function of time, as opposed to the time-independent variable $|\psi_{+1}(\xi, 0)|^2/\Lambda$ in the case of the MF model. This is a key difference, whose implications become clearer if we look at the asymptotic behavior of the total population of the forward atomic side mode. Using Eq. (16) in Eq. (12a), we obtain for $\Gamma\tau \gg 1$

$$\mathcal{N}_{+1}(\tau) \sim \frac{1}{16\pi\sqrt{\bar{\Gamma}\tau}} e^{4\sqrt{\bar{\Gamma}\tau}}, \quad (18)$$

while for the MF model one finds

$$\mathcal{N}_{+1}(\tau) \sim \frac{\eta}{8\pi\Gamma\tau} e^{4\sqrt{\Gamma\tau}}, \quad (19)$$

where we have assumed a spatially independent seeding i.e., $\psi_{+1}(\xi, 0) = \sqrt{\eta}$. Clearly, as a result of spatial propagation effects, both models predict a sub-exponential growth of the side-mode population. In the quantum model, however, the population grows like $e^{4\sqrt{\tau}}/\sqrt{\tau}$, whereas in the MF model it increases as $e^{4\sqrt{\tau}}/\tau$. The crucial point is that we cannot compensate for such a difference by assigning any constant value to the seeding η . Furthermore, the fact that the seeding appears as a prefactor in Eq. (16), suggests that any deviations of the MF atomic density profiles and populations from their quantum counterparts have to be attributed to the semiclassical nature of the MF model and not to the arbitrariness of the initial seeding, which may only lead to global changes such as a rescaling of the plotted curves. Keeping this in mind, we turn to comparing the predictions of the two models taking into account both forward and backward recoiling atoms, as well as a Thomas-Fermi distributed BEC. For direct comparison to previous work [6], we have decided to seed the mean-field model according to

$$\psi_{+1}(\xi, 0) = \psi_0(\xi)/\sqrt{N}, \quad (20)$$

which corresponds to one atom in the forward atomic sidemode distributed proportionally to the density of the BEC.

A snapshot of the atomic density profiles in the two models, after a time $\Gamma\tau = 6$, is plotted in Fig. 1. Both models predict that the profiles are peaked close to the right end of the condensate; a feature which is responsible for the experimentally observed asymmetry of the scattering pattern [6]. In the MF model, however, the profiles are peaked slightly closer to the end of the BEC, while the height and the width of the spatial distributions are underestimated, especially for the $(-)$ mode in the weak pulse regime. This discrepancy in the predictions of the two models is also reflected in the time evolution of the atomic populations in the two side modes, which are depicted in Fig. 2.

In agreement with experimental observations, both models predict that the populations of the two side modes are comparable in the strong-pulse regime, whereas in the weak-pulse regime, we have far less backwards than forwards recoiling atoms. This behavior is mathematically mirrored in the expressions for the atomic densities in the two side modes [see Eq. (15)]. They differ by one term only, which is proportional to Γ , whereas their common term scales with Γ^2 . Thus, for short times and strong pulses where $\Gamma \sim 10^2$, the two expressions become comparable, whereas they are different in the weak pulse regime

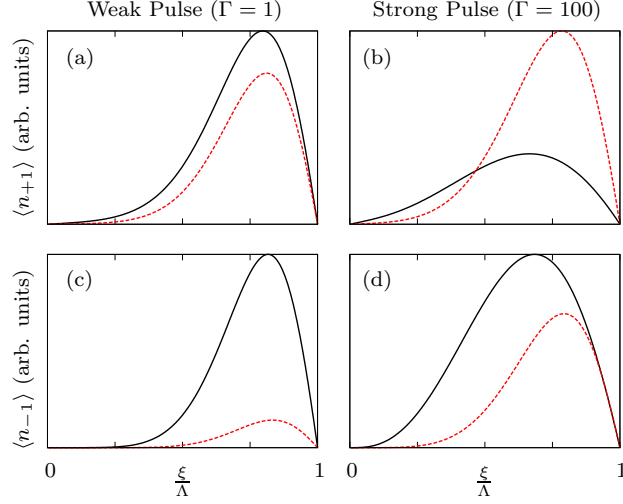


FIG. 1: (Color online) Atomic density profiles of the two side modes, according to the quantum model (black, solid) and the MF model (red, dashed), at $\Gamma\tau = 6$. The left column shows the weak pulse regime and the right column the strong pulse regime.

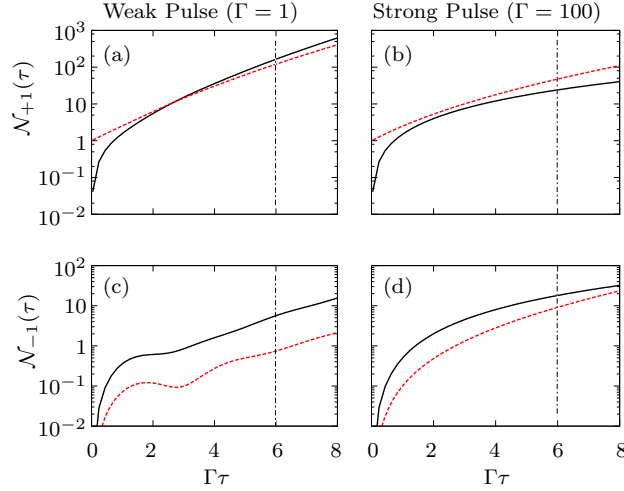


FIG. 2: (Color online) Evolution of the side-mode populations in the quantum (black, solid) and the MF (red, dashed) model. Note that the quantities are plotted on a log-scale. The dot-dashed line marks the time when the snapshots in Fig. 1 were taken.

where $\Gamma \sim 1$. It is also worth pointing out here that, as depicted in Fig. 2, the MF model gives approximately the right growth rates as well as the right qualitative behavior. In the quantum model, however, the suppression of the $(-)$ mode is not as prominent as in the MF description, and this can be attributed to the ambiguity of the seeding and therefore

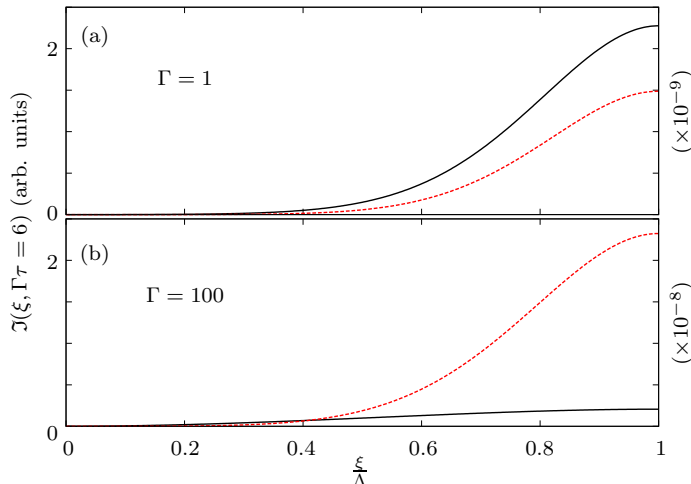


FIG. 3: (Color online) Comparison of the predictions for the photon density within the BEC in the quantum (black, solid) and the MF (red,dashes) model. The snapshots correspond to $\Gamma\tau = 6$, in the weak-pulse ($\Gamma = 1$) and the strong-pulse ($\Gamma = 100$) regimes.

the initialization of the process.

B. Scattered light

More insight into the differences between the two models is obtained by also studying the behavior of the radiation field. In the quantum model, the photon density within the BEC volume model is given by Eq. (9b), which in view of Eq. (13a) yields

$$\mathfrak{J}(\xi, \tau) = \frac{\Gamma}{\chi} \int_0^\xi d\xi' |\varphi(\xi')|^2 |F_{1,0}(\gamma_{\xi,\xi'}, \tau)|^2. \quad (21)$$

Even though this quantity cannot be measured, we will use it to compare the two models as it influences many measurable features of the process. The most easily measurable observable linked to the radiation field is the number of photons which have left the condensate up to time τ . Assuming no distracting factors between BEC and detector as well as instantaneous photon propagation, this quantity is given by Eq. (12c). Finally, it is straightforward to find the analogous quantities in the MF model using $\mathfrak{J}(\xi, \tau) = |e_+(\xi, \tau)|^2$, and again we can directly compare the predictions of the two models.

Calculations of the photon density within the BEC are plotted in Fig. 3. In the weak pulse regime, the mean-field model shows reasonable qualitative agreement with the quantum

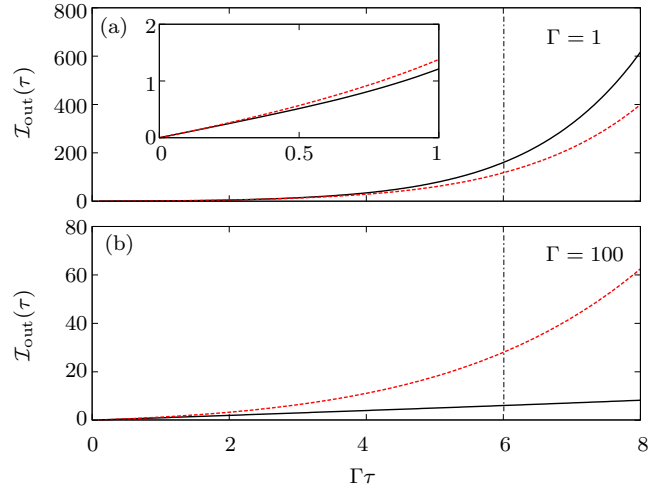


FIG. 4: (Color online) Comparison of predictions for the number of photons which have left the BEC as a function of scaled time $\Gamma\tau$ in the quantum (black, solid) and the MF (red, dashed) model. Top panel shows the weak-pulse regime ($\Gamma = 1$), while the lower panel is for the strong-pulse regime ($\Gamma = 100$). The dot-dashed line marks the time when snapshots in Fig. 3 are taken.

predictions. In the strong pulse regime, however, the quantum model predicts a much lower photon density than the MF model. This discrepancy becomes even more obvious if we look at the number of emitted photons, which is plotted in Fig. 4. While the MF model predicts a fast growth of the number of photons, the growth in the quantum model is almost linear, which in view of Eq. (12c) implies a constant density of photons within the BEC volume. Upon closer investigation, we find that such a period is also present in the weak pulse regime, albeit for shorter (scaled) times. More precisely, we find that for $\Gamma = 1$ this period lasts only until about $\tau \approx 0.5$, as can be seen in the inset of fig 4 (a).

According to our simulations, the presence of backwards recoiling atoms is suppressing superradiance. As depicted in Fig. 4, the number of scattered photons with respect to scaled time in the weak pulse regime is much higher than in the strong pulse regime, since in the latter endfire photons are destroyed on account of producing backwards recoiling atoms. This removal inhibits the fast growth of the endfire mode, which in turn is responsible for the lower scattering rate (per scaled time). In particular, the endfire mode remains weakly populated for times $\tau \lesssim \tau_c$, since in this regime, the production of backwards recoiling atoms is allowed. This behavior is consistent with the conservation law (11), which says that the number of photons outside the condensate is given by the number difference between the two

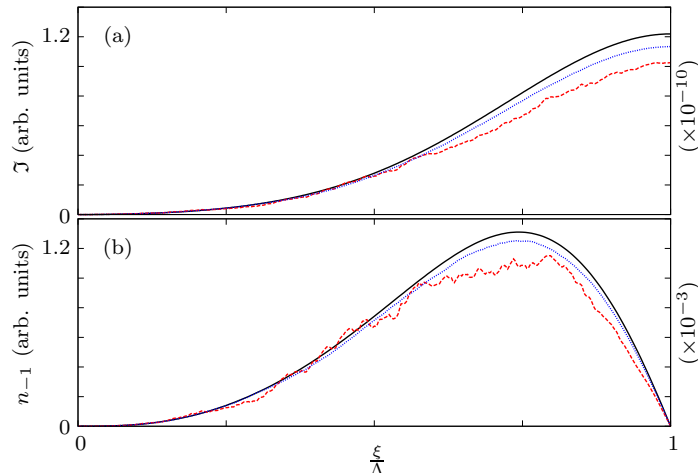


FIG. 5: (Color online) Example of photon and atom densities obtained through averaging over randomly seeded MF solutions. Figure (a) shows a snapshot of the photon density and figure (b) shows the atomic density of the (-1) mode. The quantum solution is shown in solid black, while averages over 20 and 2000 trajectories are shown in red dashed and blue dotted lines. Parameters: $\Gamma = 1$, and $\tau = 2$.

matter-wave modes. Finally we note that the suppression of the population of the endfire mode seems to be underestimated in the MF model, as can be seen from Fig. 4 (b) as well as the inset of Fig. 4 (a).

C. Averaging over semiclassical trajectories

For early times, the quantum prediction of the superradiant process is appropriate and can be expected to give better results than the MF model. It is easier, however, to perform calculations involving depletion of the BEC and population of higher modes in the MF model. It is therefore reasonable to ask, whether the quantum model is able to give us hints on how to seed the MF model appropriately to obtain quantitatively correct results. In the context of conventional superradiance, Haake *et al.* introduced the idea of averaging over many semiclassical “trajectories” to obtain quantum results [13]. The MF equations are initially seeded with random variables according to a particular distribution, while to obtain a particular quantum expectation value, one has to average over various solutions for the corresponding semiclassical quantity. We have investigated the extension of this idea to

superradiant Rayleigh scattering off BECs where, in contrast to conventional superradiance, backwards recoiling atoms are also present.

To see how this works, let us assume we want to calculate the normal-ordered n th order correlation function

$$\langle [\hat{\psi}_{-1}^\dagger(\xi_1, \tau)]^n [\hat{\psi}_{-1}(\xi_2, \tau)]^n \rangle. \quad (22)$$

From Eqs. (13) and using (4) as well as the fact that our initial state is the vacuum for all modes, we find the only non-vanishing expectation value involved to be

$$\langle \hat{\psi}_{+1}(\xi^{(1)}, 0) \dots \hat{\psi}_{+1}(\xi^{(n)}, 0) \hat{\psi}_{+1}^\dagger(\xi^{(n+1)}, 0) \dots \hat{\psi}_{+1}^\dagger(\xi^{(2n)}, 0) \rangle. \quad (23)$$

Here, the variables $\xi^{(j)}$ are integrated from 0 to ξ_1 for $j = 1, \dots, n$ and from 0 to ξ_2 for $j = n + 1, \dots, 2n$. Using the commutation relations (4), correlation (23) reads

$$\sum_{\pi} \prod_{j=1}^n \delta(\xi^{(j)} - \xi^{(n+\pi(j))}), \quad (24)$$

where δ denotes the Dirac delta and the sum runs over all permutations π of order n . Let us now seed the semiclassical model with

$$\psi_{+1}(\xi, 0) = C_{\xi}, \quad (25a)$$

$$\psi_{-1}(\xi, 0) = 0, \quad (25b)$$

$$e_+(\xi, 0) = 0, \quad (25c)$$

where C_{ξ} is a random, normally distributed complex variable, with zero mean and variance $1/\sqrt{\Delta\xi}$, with $\Delta\xi$ the spatial step of a numerical implementation. The average of the product $\psi_{+1}(\xi^{(1)}, 0) \dots \psi_{+1}(\xi^{(n)}, 0) \psi_{+1}^*(\xi^{(n+1)}, \tau) \dots \psi_{+1}^*(\xi^{(2n)}, 0)$ over many trajectories (seedings) will effectively converge towards a discretized version of Eq. (24). Due to the formal equivalence of the semiclassical solutions to the quantum ones, the product $\psi_{-1}(\xi_1, \tau)^n \psi_{-1}(\xi_2, \tau)^n$ will consequently converge to the quantum expectation value (22). To find correlation functions of other operators, other seedings have to be used, which can be found in an analogous way. Table I summarizes these relationships.

As far as densities and populations are concerned, the convergence of the averaging procedure towards the quantum solution is fairly fast. For instance, as depicted in Fig. 5, one typically has to average over a couple of thousand trajectories, to obtain well converged, smooth density profiles. We note that the curves lie generally below the quantum mechanical

| Quantum Operator | Seeded Fields |
|------------------------------|--|
| $\hat{e}_+(\xi, \tau)$ | $\psi_{+1}(\xi', 0)$ |
| $\hat{\psi}_{+1}(\xi, \tau)$ | $\psi'_{-1}(\xi', 0)$ $e_+(0, \tau')$ |
| $\hat{\psi}_{-1}(\xi, \tau)$ | $\psi_{+1}(\xi', 0)$ |

TABLE I: Summary of relations between quantum mechanical expectation values and random initial seeds to the mean-field model.

results. This is, however, a purely numerical effect, and it disappears when the number of trajectories increases. For a sufficiently large sample of trajectories, we hence also have true numerical convergence. Clearly, the averaging procedure is also applicable to correlations of higher order. One can calculate any normal ordered correlation function of the system by averaging over a sufficiently large ensemble of MF trajectories, provided that the operators involved in the correlation function have the same seeding requirements. The convergence, however, becomes rapidly slower with every order added, such that higher order correlations will require a larger number of trajectories.

V. RESULTS BEYOND THE MEAN FIELD MODEL

A. Population Ratio

An easily accessible quantity in a BEC superradiance experiment is the ratio of backwards to forwards recoiling atoms. In the quantum model, the calculation of this quantity is straight forward and unambiguous. From Eqs. (15) and (12a) we find

$$\frac{\mathcal{N}_{-1}(\tau)}{\mathcal{N}_{+1}(\tau)} = \left[1 + \frac{\int_0^\Lambda d\xi \int_0^\tau d\tau' |\varphi(\xi)|^2 |F_{1,0}(\gamma_{\xi,0}, \tau')|^2}{\Gamma \int_0^\Lambda d\xi \int_0^\xi d\xi' |\varphi(\xi)|^2 |\varphi(\xi')|^2 |F_{1,1}(\gamma_{\xi,\xi'}, \tau)|^2} \right]^{-1}. \quad (26)$$

One cannot expect the MF model to deliver reliable results for such a quantity, due to its ambiguous initialization related to the seeding. To find out how different the predictions of the two models for this ratio are, the MF equations of motion were seeded according to Eq. (20), and the predictions of both models for the time evolution of the ratio in the two regimes are plotted in Fig. 6.

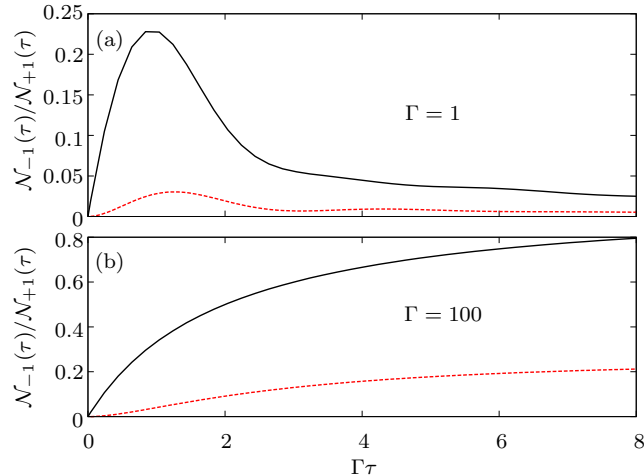


FIG. 6: (Color online) Time evolution of the ratio of backwards to forwards recoiling atoms as a function of scaled time in the quantum (black, solid) and the MF (red, dashed) model, for the weak-pulse (a) and the strong pulse (b) regimes.

Let us recall here that according to experimental observations, the population of the backwards atomic sidemodes is highly suppressed in the weak-pulse regime. Our quantum theoretical predictions reproduce these observations, i.e. the ratio is closer to one in the strong-pulse regime. In the MF model, it never exceeds 0.3 throughout its evolution in either of the two regimes, even though it does attain higher values for strong couplings. As discussed in Sec. II, the suppression of backwards recoiling atoms due to the energy mismatch is expected to set in at $\tau \approx \tau_c$. Indeed, as depicted in Fig. 6, in the weak pulse regime the ratio of backwards to forwards recoiling atoms drops for times $\tau \gtrsim \tau_c$. In the strong-pulse regime, however, and for the time scales consistent with the validity of our model, we are always well below τ_c , and the ratio increases monotonically. Nevertheless, even in this case, the onset of the suppression manifests itself in the temporal behavior of the growth rate of the ratio. Finally, it is also worth noting that the evolution of the ratio in the weak-pulse regime agrees qualitatively with the corresponding results in [7]. A quantitative comparison, however, is rather difficult due to different definitions of the coupling strength.

B. Coherence of the scattered light

Another class of questions typically addressed in a superradiance experiment pertains to the properties of emitted light. Of particular interest are the coherence properties which are described through correlation functions and are also accessible to measurements. For instance, the first-order correlation function $G^{(1)}(\tau, T) = \langle \hat{e}_+^\dagger(\Lambda, \tau + T) \hat{e}_+(\Lambda, \tau) \rangle$, describes the temporal coherence properties of the light that are relevant to an experiment of the Young's type, where the light at two times (i.e., at τ and $\tau + T$) is superimposed to produce interference patterns [14]. The visibility of the fringes in the observed pattern is proportional to the degree of first-order coherence, defined as

$$g^{(1)}(\tau, \tau + T) = \frac{G^{(1)}(\tau, \tau + T)}{\sqrt{\mathfrak{J}(\Lambda, \tau + T)\mathfrak{J}(\Lambda, \tau)}}. \quad (27)$$

On the other hand, intensity correlations are described through the normalized second order correlation function defined as [14]

$$g^{(2)}(\tau, \tau + T) = \frac{\langle \hat{e}_+^\dagger(\Lambda, \tau) \hat{e}_+^\dagger(\Lambda, \tau + T) \hat{e}_+(\Lambda, \tau) \hat{e}_+(\Lambda, \tau + T) \rangle}{\mathfrak{J}(\Lambda, \tau)\mathfrak{J}(\Lambda, \tau + T)}. \quad (28)$$

This quantity is basically related to the probability of detecting a photon at time $\tau + T$, given that a photon was detected at time τ . Definitions (27) and (28) are general and applicable to any light source, but can be simplified considerably for stationary sources, where the properties of the light depend only on the *delay time* T . Actually, this is the case typically discussed in standard text books [14]. In the present setting, however, the process is by no means stationary, and thus well known expressions and conclusions are not necessarily applicable to our case.

Using Eqs. (13), one obtains

$$g^{(2)}(\tau, \tau + T) = 1 + |g^{(1)}(\tau, \tau + T)|^2, \quad (29a)$$

where

$$G^{(1)}(\tau, \tau + T) = \int_0^\Lambda d\xi |\psi_0(\xi)|^2 F_{1,0}(\gamma_{\Lambda,\xi}, \tau) F_{1,0}^*(\gamma_{\Lambda,\xi}, \tau + T), \quad (29b)$$

while $\mathfrak{J}(\xi, \tau)$ is given by Eq. (21).

Equation (29a) is a typical property of so-called chaotic light sources [14], albeit in our case the source is non stationary. Indeed, as depicted in Fig. 7, even within the undepleted pump approximation adopted throughout this work, for a given delay time T , $g^{(2)}(\tau, \tau + T)$

depends crucially on τ . In view of Eq. (29), we have $g^{(2)}(\tau, \tau) = 2$ for all τ , which is a manifestation of intensity correlations. In other words, the endfire photons tend to appear bunched and thus detecting a photon at time τ , significantly increases the probability of detecting another photon simultaneously. On the other hand, as $T \rightarrow \infty$ we obtain $g^{(2)}(\tau, \tau + T) \rightarrow 1$, indicating that the intensities are uncorrelated for large delay times. Typically, these asymptotic behaviors of $g^{(2)}(\tau, \tau + T)$ are defined with respect to the characteristic coherence time T_c of the light under investigation (i.e., $T \rightarrow 0$ and $T \rightarrow \infty$ refer to $T \ll T_c$ and $T \gg T_c$, respectively). Unfortunately, the validity of the present model restricts us to relatively small times, and we cannot provide quantitative estimates of the coherence time T_c . Nevertheless, we can still draw some conclusions about the behavior of $g^{(2)}(\tau, \tau + T)$ in the weak and in the strong pulse regimes. Before this, it is also worth pointing out that measuring the correlation function in dependence of the delay time T (irrespective of τ) would facilitate any experiment considerably. In practice, this can be achieved, for instance, by forming blocks of data pertaining to various τ but the same delay time T , and then estimate $\tilde{g}^{(2)}(T)$ based on these blocks. Formally, this procedure corresponds to the time averaged degree of second order coherence given by

$$\tilde{g}^{(2)}(T) = \frac{\int_0^{\tau_0} d\tau \langle \hat{e}_+^\dagger(\Lambda, \tau) \hat{e}_+^\dagger(\Lambda, \tau + T) \hat{e}_+(\Lambda, \tau) \hat{e}_+(\Lambda, \tau + T) \rangle}{\int_0^{\tau_0} d\tau \mathfrak{J}(\Lambda, \tau) \mathfrak{J}(\Lambda, \tau + T)}, \quad (30)$$

where τ_0 denotes the time over which experimental data are collected. This expression is analogous to volume integrated correlation functions used in [15]. Note that when there is no dependence on τ , Eq. (30) reduces to the standard expression of $\tilde{g}^{(2)}(T)$ for stationary sources [14].

As depicted in Fig. 8, the behavior of $\tilde{g}^{(2)}(T)$ is substantially different in the weak and the strong pulse regimes. While in the weak pulse regime the correlation function seems to decay slowly but steadily, in the strong pulse regime we clearly have two stages. The initial transient regime is characterized by a rapid drop of $\tilde{g}^{(2)}(T)$, which is followed by a regime of very slow decay. To a good approximation $\tilde{g}^{(2)}(T)$ decreases linearly with increasing delay times, in both regimes. Moreover, according to Fig. 8, the tendency of photons to arrive in bunches is much lower in the strong pulse regime than in the weak pulse regime. This behavior can be attributed to the production of backwards recoiling atoms at the expense of endfire photons (see red curve). Intensity correlation function can thus be viewed as a measure of the contribution of backwards recoiling atoms to the total number of scattering events.

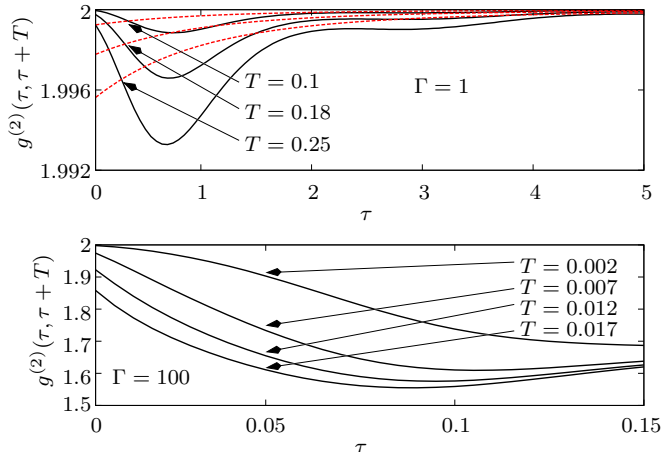


FIG. 7: (Color online) Behavior of the photon intensity correlation $g^{(2)}(\tau, \tau + T)$ as a function of τ for various fixed delays T as given in the figures. The dashed line in the top figure gives the same function neglecting the (-1) mode.

In this context, we can also interpret the behavior of $g^{(2)}(\tau, \tau + T)$ as a function of τ . As depicted in Fig. 7, for both regimes there seems to be a systematic temporal behavior of $g^{(2)}(\tau, \tau + T)$ for a given delay time. The correlation function decreases for short times, while for larger times it increases (at least in the weak pulse regime). Such a behavior reflects changes in the statistical properties of the source, which can be also associated with the production of backward recoiling atoms. Indeed, as depicted in Fig. 7, neglecting the backward mode $(-)$ in our equations of motion, one finds a monotonic behavior of $g^{(2)}(\tau, \tau + T)$ (in good qualitative agreement with predictions for conventional superradiance [16]). For short times, photons that have been scattered into the endfire mode are consumed during the production of backward recoiling atoms which, as discussed in Sec. II, can take place for times shorter than τ_c . This is also confirmed by the fact that according to Fig. 7, in the weak pulse regime for a given T , $g^{(2)}(\tau, \tau + T)$ exhibits a minimum for times very close to τ_c . In the strong-pulse regime, although our time scales are always well below τ_c , the onset of suppression manifests itself in the minimum of the intensity correlation function. To complete the picture, it is important to note here that superradiant Rayleigh scattering off BECs basically involves the mixing of optical and matter waves, which is a nonlinear process. Thus, any changes in the densities and/or populations of the fields that are mixed, are expected to affect considerably the statistics of the scattered light.

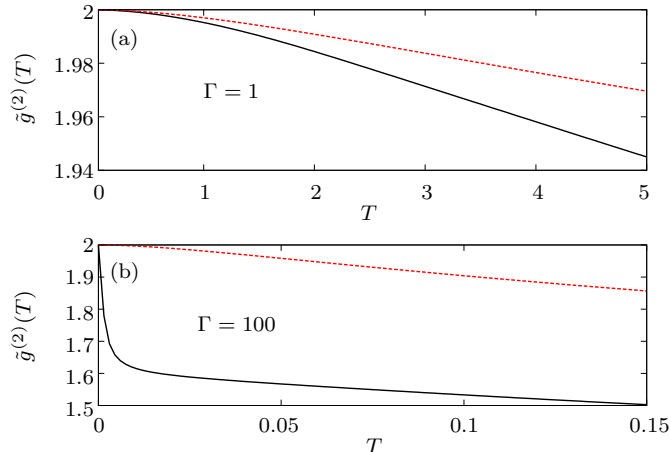


FIG. 8: (Color online) Integrated correlation function $\tilde{g}^{(2)}(T)$ as a function of the delay time T for the weak (top) and strong (bottom) pulse regime. Dashed line in the top figure is the same function neglecting backwards recoiling atoms.

VI. CONCLUSIONS

We have discussed the early stage of superradiant Rayleigh scattering off atomic condensates, in the framework of a quantum model that takes into account spatial effects. Exact analytic solutions to this model can be expressed in terms of integrals involving Bessel functions, and are substantially different from the corresponding semiclassical solutions that have been obtained previously in the context of a related mean-field model. Nevertheless, the predictions of the two models about density profiles and growth rates are in reasonable qualitative agreement. An exception to this behavior is a strong suppression of photonic endfire modes at early times, which is underestimated in the mean-field treatment. For a large collection of condensed atoms, the effect of quantum fluctuations on various observable quantities can be obtained by averaging over ensembles of semiclassical trajectories. Each trajectory corresponds to the solution of the mean-field equations of motion, where an appropriate random seeding has been used. Hence histograms of a particular observable will reveal its distribution according to the quantum model. This technique will be used in future work to study photon delay time statistics. The quantum predictions for the ratio of backward to forward recoiling atoms is in qualitative agreement with experimental observations as well as other theoretical treatments. Finally, the present model enabled us to calculate the statistical behavior of scattered photons, which is qualitatively different in

the Kapitza-Dirac and Bragg regimes. This difference can be attributed to the suppression of photonic endfire modes due to the large number of back-scattered atoms at early times. In both regimes, the presence of backscattering distinguishes the photon statistics from the ones observed in conventional superradiance.

VII. ACKNOWLEDGEMENT

This work was supported by the EC RTN EMALI (Contract No. MRTN-CT-2006-035369).

Appendix A: Solving the Equations of Motion

To find solutions to Eqs. (5), we first apply the Laplace transform with respect to $\tau \rightarrow p$ to all three equations and find

$$\mathcal{L}_{\tau \rightarrow p}\{\hat{\psi}_{+1}^\dagger(\xi, \tau)\} = \frac{1}{p} \left[\hat{\psi}_{+1}^\dagger(\xi, 0) + i\kappa\psi_0^*(\xi)\mathcal{L}_{\tau \rightarrow p}\{\hat{e}_+(\xi, \tau)\} \right], \quad (\text{A1a})$$

$$\mathcal{L}_{\tau \rightarrow p}\{\hat{\psi}'_{-1}(\xi, \tau)\} = \frac{1}{p + 2i} \left[\hat{\psi}'_{-1}(\xi, 0) - i\kappa\psi_0(\xi)\mathcal{L}_{\tau \rightarrow p}\{\hat{e}_+(\xi, \tau)\} \right], \quad (\text{A1b})$$

$$\begin{aligned} \chi \frac{\partial}{\partial \xi} \mathcal{L}_{\tau \rightarrow p}\{\hat{e}_+(\xi, \tau)\} &= -p\mathcal{L}_{\tau \rightarrow p}\{\hat{e}_+(\xi, \tau)\} + \hat{e}_+(\xi, 0) \\ &\quad - i\kappa \left[\psi_0(\xi)\mathcal{L}_{\tau \rightarrow p}\{\hat{\psi}_{+1}^\dagger(\xi, \tau)\} + \psi_0^*(\xi)\mathcal{L}_{\tau \rightarrow p}\{\hat{\psi}'_{-1}(\xi, \tau)\} \right]. \end{aligned} \quad (\text{A1c})$$

After inserting (A1a) and (A1b) in Eq. (A1c) we are left with a differential equation of the form

$$\frac{\partial}{\partial \xi} \mathcal{L}_{\tau \rightarrow p}\{\hat{e}_+(\xi, \tau)\} = -\mathbf{a}(\xi, p)\mathcal{L}_{\tau \rightarrow p}\{\hat{e}_+(\xi, \tau)\} - \mathbf{b}(\xi, p), \quad (\text{A2})$$

which has the solution

$$\mathcal{L}_{\tau \rightarrow p}\{\hat{e}_+(\xi, \tau)\} = e^{-\int_0^\xi d\xi' \mathbf{a}(\xi', p)} \mathcal{L}_{\tau \rightarrow p}\{\hat{e}_+(0, \tau)\} - e^{-\int_0^\xi d\xi' \mathbf{a}(\xi', p)} \int_0^\xi d\xi' e^{-\int_0^\xi d\xi'' \mathbf{a}(\xi'', p)} \mathbf{b}(\xi', p). \quad (\text{A3})$$

This expression can be inserted in Eqs. (A1a, A1b), at which point we have closed expressions for all three Laplace transformed fields. The remaining inversion of the Laplace transforms can be found using elementary techniques given in e.g. [17]. The solutions are expressed in terms of the following functions

$$F_{0,0}(y, z) = \delta(z) + \Theta(z) \sqrt{\frac{y}{z}} I_1(2\sqrt{yz}) - \Theta(z) e^{-2iz} \sqrt{\frac{y}{z}} J_1(2\sqrt{yz'}) \quad (\text{A4a})$$

$$- \Theta(z) y \int_0^z dz' e^{-2iz'} \frac{I_1(2\sqrt{y(z-z')}) J_1(2\sqrt{yz'})}{\sqrt{(z-z')z'}}, \quad (\text{A4b})$$

$$F_{1,0}(y, z) = I_0(2\sqrt{yz}) \Theta(z) - \Theta(z) \sqrt{y} \int_0^z dz' \frac{e^{-i2z'}}{\sqrt{z'}} I_0[2\sqrt{y(z-z')}] J_1(2\sqrt{yz'}), \quad (\text{A4c})$$

$$F_{0,1}(y, z) = e^{-2iz} J_0(2\sqrt{yz}) \Theta(z) + \Theta(z) \sqrt{y} \int_0^z dz' \frac{e^{-i2z'}}{\sqrt{z-z'}} I_1[2\sqrt{y(z-z')}] J_0(2\sqrt{yz'}), \quad (\text{A4d})$$

$$F_{1,1}(y, z) = \Theta(z) \int_0^z dz' e^{-i2z'} I_0[2\sqrt{y(z-z')}] J_0(2\sqrt{yz'}), \quad (\text{A4e})$$

$$F_{2,0}(y, z) = \sqrt{\frac{z}{y}} I_1(2\sqrt{yz}) \Theta(z) - \Theta(z) \int_0^z dz' e^{-2iz'} \sqrt{\frac{z-z'}{z'}} I_1[2\sqrt{y(z-z')}] J_1[2\sqrt{yz'}], \quad (\text{A4f})$$

$$F_{0,2}(y, z) = e^{-2iz} \sqrt{\frac{z}{y}} J_1(2\sqrt{yz}) \Theta(z) + \Theta(z) \int_0^z dz' e^{-2iz'} \sqrt{\frac{z'}{z-z'}} I_1[2\sqrt{y(z-z')}] J_1[2\sqrt{yz'}], \quad (\text{A4g})$$

with J_i and I_i the i th Bessel function of the first kind and the i th modified Bessel function respectively. They satisfy the recursion relations

$$\begin{aligned} \frac{\partial}{\partial u} F_{\mu,\nu}(u, v) &= F_{\mu+1,\nu}(u, v) - F_{\mu,\nu+1}(u, v), \\ \frac{\partial}{\partial v} F_{\mu,\nu}(u, v) &= 2F_{\mu-1,\nu}(u, v), \\ 2iF_{\mu,\nu}(u, v) &= F_{\mu,\nu-1}(u, v) - F_{\mu-1,\nu}(u, v), \end{aligned} \quad (\text{A5})$$

which are a consequence of properties of the Laplace transform. For the solutions with neglected backwards scattering, we use the functions

$$F_0(y, z) = \delta(z) + \Theta(z) \sqrt{\frac{y}{z}} I_1(2\sqrt{yz}) \quad (\text{A6})$$

$$F_1(y, z) = \Theta(z) I_0(2\sqrt{yz}) \quad (\text{A7})$$

$$F_2(y, z) = \Theta(z) \sqrt{\frac{z}{y}} I_1(2\sqrt{yz}). \quad (\text{A8})$$

[1] R. H. Dicke, Phys. Rev. **93**, 99 (1954).

- [2] N. Skribanowitz, I. P. Herman, J. C. MacGillivray and M. S. Feld, Phys. Rev. Lett. **30**, 309 (1973); Q. H. F. Vreken, H. M. J. Hikspoors and H. M. Gibbs, Phys. Rev. Lett. **38**, 764 (1977); Y. N. Chen, D. S. Chuu and T. Brandes, Phys. Rev. Lett. **90**, 166802 (2003); Y. N. Chen, C. M. Li, D. S. Chuu and T. Brandes, New J. Phys. **7**, 172 (2005); A. Mitra, R. Vyas and D. Erenso, Phys. Rev. A **76**, 052317 (2007).
- [3] M. Gross and S. Haroche, Phys. Rep. **93**, 301 (1982).
- [4] N. Piovella, R. Bonifacio, B. W. J. McNeil and G. R. M. Robb, Opt. Commun. **187**, 165 (2001); C. Benedek and M. G. Benedict, J. Opt. B. **6**, S111 (2004).
- [5] Ö. E. Müstecaplıoğlu and L. You, Phys. Rev. A **62**, 063615 (2000); Yu. A. Avetisyan and E. D. Trifonov, Laser Phys. Lett. **1**, 373 (2004).
- [6] O. Zobay and Georgios. M. Nikolopoulos, Phys. Rev. A **73**, 013620 (2006); O. Zobay and G. M. Nikolopoulos, *ibid* **72**, 041604(R) (2005); O. Zobay and G. M. Nikolopoulos, Laser Phys. **17**, 180 (2007).
- [7] M. G. Moore and P. Meystre, Phys. Rev. Lett. **83**, 5202 (1999); H. Pu, W. Zhang, and P. Meystre, Phys. Rev. Lett. **91**, 150407 (2003).
- [8] X. Zhou, F. Yang, X. Yue, T. Vogt and X. Chen, Phys. Rev. A **81**, 013615 (2010); A. Hilliard, F. Kaminski, R. leTargat, C. Olausson, E. S. Polzik and J. H. Müller, Phys. Rev. A **78**, 051403(R) (2008); F. Yang, X. Zhou, J. Li, Y. Chen, L. Xia and X. Chen, Phys. Rev. A **78**, 043611 (2008); N. Bar-Gill, E. E. Rowen and N. Davodson, Phys. Rev. A **76**, 043603 (2007).
- [9] S. Inouye, A. P. Chikkatur, D. M. Stamper-Kurn, J. Stenger, D. E. Pritchards, W. Ketterle, Science **285**, 571 (1999) D. Schneble, Y. Torii, M. Boyd, E. W. Streed, D. E. Pritchard and W. Ketterle, Science **300**, 475 (2003).
- [10] J. M. Vogel, K. Xu and W. Ketterle, Phys. Rev. Lett. **89**, 020401 (2002).
- [11] L. F. Buchmann, G. M. Nikolopoulos, O. Zobay and P. Lambropoulos, Phys. Rev. A **81**, 031606(R) (2010).
- [12] W. Zhang and D. F. Walls, Phys. Rev. A **49**, 3799 (1994)
- [13] F. Haake, H. King, G. Schröder, J. Haus and R. Glauber, Phys. Rev. A **20**, 2047 (1979); F. Haake, J. W. Haus, H. King, G. Schröder and R. Glauber, Phys. Rev. A **23**, 1322 (1981).
- [14] M. O. Scully and M. S. Zubairy, *Quantum Optics*, (Cambridge University Press 1997).
- [15] M. Naraschewski and R. J. Glauber, Phys. Rev. A **59**, 4595 (1998)
- [16] Mihaly G, Benedict *et al.*, *Super-Radiance* (Taylor & Francis Group, New York, 1996)

- [17] M. Abramovitz and I. A. Stegun, eds. *Handbook of Mathematical Functions with Formulas, Graphs, and Mathematical Tables* (Dover, New York 1964)
- [18] Since the fields of interest vary slowly on length scales $1/k$, we can approximate the $\delta_\Delta(z)$ distributions by Dirac delta functions